Proceedings of Global Power and Propulsion Society
ISSN-Nr: 2504-4400
GPPS Xi'an21
18th – 20th October, 2021
www.gpps.global

GPPS-TC-2021-0105

A FLUID-THERMAL ANALYSIS OF PARTIAL ADMISSION AXIAL TURBINES

Hanwei Wang
School of Marine Science and Technology, Northwestern Polytechnical University
wanghanwei@mail.nwpu.edu.cn
Xi'an, Shaanxi, China

Kai Luo
School of Marine Science and Technology, Northwestern Polytechnical University
nwpu_wyh@nwpu.edu.cn
Xi'an, Shaanxi, China

Qiushi Yang
School of Marine Science and Technology, Northwestern Polytechnical University
2019200465@mail.nwpu.edu.cn
Xi'an, Shaanxi, China

Chuang Huang
School of Marine Science and Technology, Northwestern Polytechnical University
huangchuang@nwpu.edu.cn
Xi'an, Shaanxi, China

Kan Qin[1]
School of Marine Science and Technology, Northwestern Polytechnical University
kan.qin@nwpu.edu.cn
Xi'an, Shaanxi, China

ABSTRACT

The partial admission axial turbines operate with the extreme pressure, temperature, and rotational speed for underwater applications. The thermal stress and mechanical stress need to be carefully examined to avoid the operation failure. In this paper, a two-way weakly fluid-thermal analysis is performed to attain the rotor disk temperature distribution. The fluid simulation is performed by solving the three-dimensional Reynolds averaged Navier-Stokes equations coupled with k-omega SST turbulence model, while the thermal analysis is conducted using the finite element method. The mixing plane method is applied when transferring the temperature due to the partial admission configuration. Once the steady state temperature distribution is achieved, the pressure distribution and centrifugal forces are also applied as the aerodynamic and mechanical loads. The corresponding stress and deformation are subsequently obtained. The results show that the maximum stress at the operating point exceeds the allowable material stress, indicating a proper cooling strategy is needed for future investigations.

INTRODUCTION

Underwater vehicles are now widely used for the ocean exploration (French, 2010). Compared to the electrical power system, the turbine power system presents a higher energy density, and it is beneficial to increase the operational range and speed for underwater vehicles (Qin et al., 2020; Wang et al., 2021). To further enhance the corresponding range and speed, increasing the turbine output power and efficiency is necessary. The previous study has shown that a 56 K increment of the turbine inlet temperature can result in an 8-13% increase in output power and 2-4% increase in cycle efficiency (Bunker, 2013). In addition, a high turbine inlet temperature can maintain the core size down (Moustapha et al., 2003). This is particularly essential for underwater vehicles, where the space is limited. However, increasing turbine inlet temperature can also create more severe operating conditions and the turbine operating safety is then significantly influenced. Hence, it is first necessary to accurately obtain the temperature and stress distribution of the turbine wheel for future cooling assessment.

The conjugate heat transfer (CHT) simulations can be employed to present the glimpse into the turbine thermal performance. Two methods are available to solve CHT problems. The first one is to use the same solver to calculate fluid and solid domains simultaneously, for example NASA's Glenn-HT solver (Rigby and Lepicovsky, 2001). The other method is to use different solver to calculate fluid and solid domains separately, such as CHT-Flow solver (Bohn et al.,

[1] Corresponding author: kan.qin@nwpu.edu.cn

1999). These two methods are still widely applied to solve CHT problems (Bohn et al., 2021; Ju et al., 2021). For partial admission turbines, since the flow characteristic is strongly unsteady, the rotation effects must be considered to accurately capture the temperature distribution in the calculation process. For a turbine with the rotational speed of 50,000 rpm, it takes only 1.2 ms per one revolution, while the time constants in the heat conduction problems are significantly large (usually of the order of minutes (Qin et al., 2018)). As shown in Ref. (Shrestha et al., 2013), it is experimentally determined that 3000 s is needed to reach the thermal equilibrium state. Therefore, it is inappropriate to use strong coupling method for thermal analysis of partial admission turbines. The steady-state solution method in the solid domain is more appropriate and a weakly coupling between the fluid and heat conduction solvers is implemented. Although it is difficult to obtain the wall temperature variation with time, the steady-state temperature distribution can be obtained by averaging the data at the circumferential direction.

The remainder of this paper is organized as follows. The numerical and fluid-thermal method is first introduced followed by the model validation. The temperature, stress and deformation analysis of the partial admission axial turbine is then detailed.

METHODOLOGY

Numerical Method

For fluid simulations, the ANSYS Fluent 18.2 solver with SIMPLEC algorithm is used (ANSYS, 2017). The SST (Shear Stress Transfer) k-ω turbulence model is selected to close Reynolds-averaged Navier-Stokes (RANS) equations and the viscous heating effect is also considered. In addition, the convergence criterion is based on the difference between two consecutive iterations of the total-to-static efficiency (less than 0.01). The ANSYS Mechanical APDL is used for thermal and structural analysis, where the Distributed Sparse Matrix Solver is used for steady-state thermal analysis and the Preconditioned Conjugate Gradient (PCG) solver is used for the steady-state structure analysis. In addition, the convergence tolerance of 10^{-7} is selected.

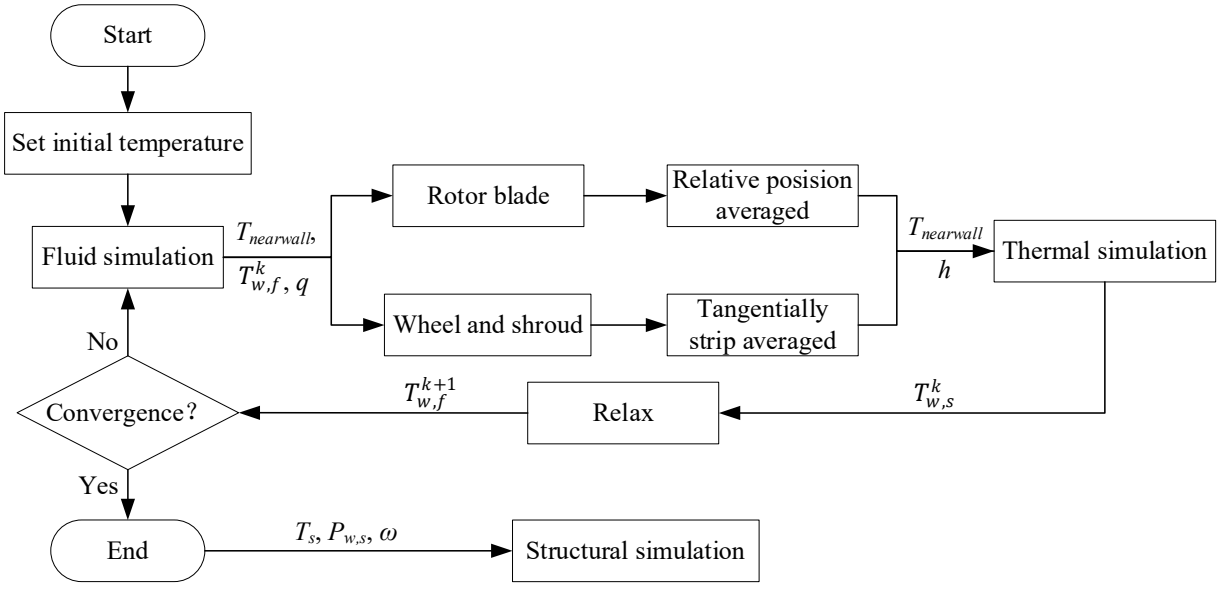

Figure 1 Schematic Diagram of Fluid-thermal Simulation Procedure

The two-way weakly fluid-thermal simulation procedure is shown in Figure 1. The wall temperature is initially prescribed. Typically, the uniform temperature is set for all rotor walls. Since the cooling water temperature is 318 K in the bearing and the rotor temperature is higher. Therefore, 318 K is set as the initial temperature for all rotor walls. The whole simulation procedure is:

1. The fluid domain with the initial wall temperature $T_{w,f}^{k}$ is solved until the steady state is achieved.

2. The heat flux q and near wall temperature $T_{nearwall}$ at the fluid-solid interfaces are extracted from the fluid domain. $T_{nearwall}$ is the local fluid temperature adjacent to the wall at the first layer of the mesh.

3.The heat flux is then mapped from the fluid domain to solid domain. As the rotor is spinning, a mixing-plane or tangentially strip averaged boundary conditions is applied during data transfer. In this way, the heat flux q and near wall temperature $T_{nearwall}$ at the fluid domain is averaged in the tangential direction when passed to the solid interface for wheel and shroud. For the rotor blade, it is averaged at the relative same node of different blade because the grid is modeled by rotation and the nodes position of each rotor is relatively the same. The convective heat transfer coefficient h is then calculated as:

$$h = \frac{q}{T_{nearwall} - T_{w,f}^{k}} \qquad (1)$$

4. The convective heat transfer coefficient and $T_{nearwall}$ are then taken as the boundary condition for the heat conduction analysis. The temperature distribution in the solid domain is solved until the solution is converged.

5. The wall temperature $T_{w,s}^{k}$ at the interfaces from the thermal simulation is extracted. The new wall temperature $T_{w,f}^{k+1}$ as the boundary condition for fluid simulation is then used (equation (2)). The under-relaxation factor β is set as 0.3 in this paper.

$$T_{w,f}^{k+1} = T_{w,f}^{k} + \beta\left(T_{w,s}^{k} - T_{w,f}^{k}\right) \qquad (2)$$

6. Repeat steps 1-5 using the new $T_{w,f}^{k+1}$ until convergence.

7. The solid temperature T_s, wall pressure P_s and rotation speed ω are then transformed to the structural simulation. This is to obtain the corresponding stress and deformation.

For the interface data transformation, the profile preserving transfer is applied to control the accuracy during data transfers. In addition, the bucket surface search algorithm is used to locate a source element that each target node can be mapped to. The triangulation method is selected as the weighting type. Typically, 40 iteration loops are needed to obtain the converged solution.

Model Validation

The supersonic flow inside a cooled axisymmetric convergent divergent nozzle is used as the validation case. The analysis is based on the experimental data reported in Ref.(Back et al., 1964). The detailed geometry and operating condition are illustrated in Figure 2 (DeLise and Naraghi, 1995; Marineau et al., 2006).

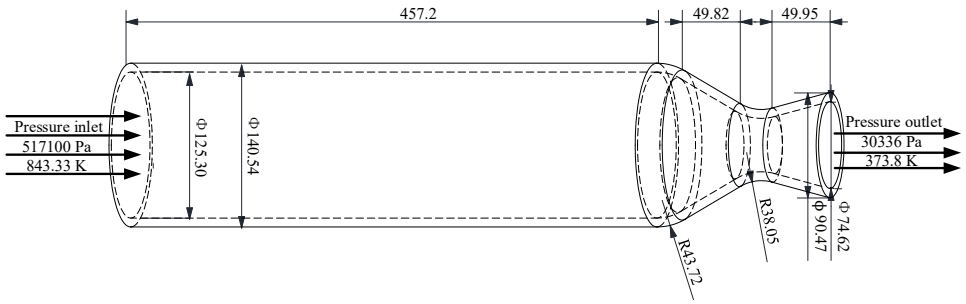

Figure 2 Geometry and Operating Condition for supersonic flow inside a cooled axisymmetric nozzle.

The temperature distribution for the outer wall of the nozzle measured during the experiment is shown in Figure 3 a). This is used as the nonuniform temperature boundary for the outer wall in the numerical simulation. In addition, the thermal conductivity of the nozzle wall is approximately 27 W/m·K (Marineau et al., 2006). Figure 3 b) shows the comparison between predicted inner wall temperatures and experimental data. The predicted wall temperatures are close to the experimental values.

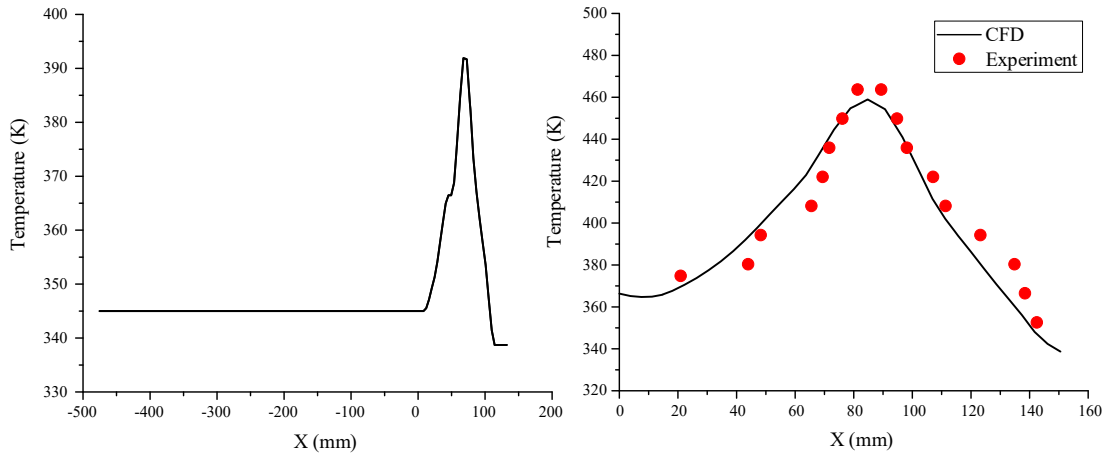

a) input b) result

Figure 3 a) Temperature Input at Outer Wall; b) Temperature Comparation at Inner Wall

RESULTS AND DISCUSSION

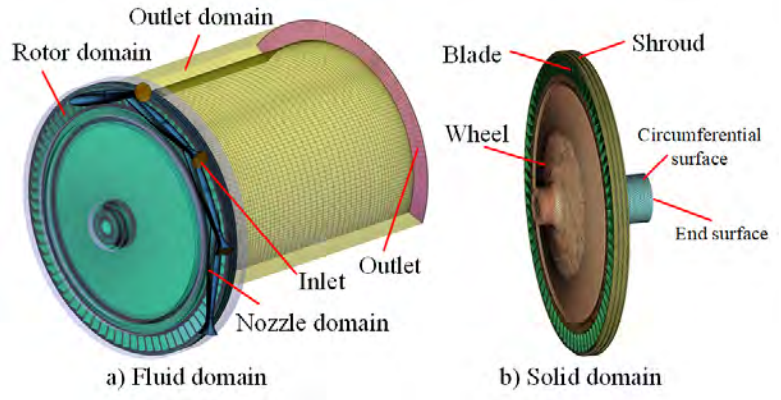

Figure 4 Computational Domain of Partial Admission Turbines

To assess the thermal performance for partial admission turbines without any cooling strategy, the operating condition at the design point is selected. The boundary conditions are listed in Table 1 and the computational domain is shown in Figure 4. The whole fluid and solid domains are modeled. The steady state simulation is used to reduce the computational cost. Due to the transient effects, the mixing plane is applied at the interface between fluid and solid domains during data transfer. In addition, a large amount of cooling water is assumed to spray on the shaft circumferential surface, therefore the circumferential surface of the shaft is approximately determined by the temperature of the liquid water (318.15 K). For the shaft end surface temperature, the bearing lubricating oil temperature (353.13K) is selected as the boundary temperature.

Table 1 Boundary Conditions

Location	Boundary Conditions
Fluid domain	
Nozzle inlet	Total pressure 19MPa Total temperature 1373 K
Out domain outlet	Static pressure 0.23 MPa
Rotor domain	Rotation, 49762 rpm
Nozzle domain	Stationary
Out domain	Stationary
Interface of the stator and rotor	Frozen rotor
Interface of the rotor and outlet	
Rotor walls (blade and wheel)	Temperature distribution from solid domain, no slip
Other walls (turbine casing)	Adiabatic, no slip
Fluid	Ideal gas, k = 1.222, R = 0.3698 kJ/kg·K
Solid domain	
Circumferential surface of the shaft	Constant temperature 318.15 K
End surface of the shaft	Constant temperature 353.15 K, fixed support
Rotor walls	Convection heat transfer coefficient distribution from fluid domain Pressure distribution from fluid domain
Material	ρ = 8.226 g/cm^3, E = -0.0584T + 232.6, $\mu \approx$ 0.4, α = 0.0056T + 8.6763, λ = 0.0108T + 5.7129

Heat Transfer Characteristic

The temperature distributions at rotor walls are depicted in Figure 5. The rotor temperatures are smeared circumferentially due to the high-speed rotor rotation. One of the reasons for the temperature increase in the radial direction of the wheel, is due to the increase in the wheel velocity (viscous heating effects, front: 513W and back: 722W). However, the main reason for the high wall temperature at the front side is due to the mixing effect from the high temperature leakage gas (0-60mm). The convection heat transfer of the leaking gas becomes significant from 60mm to 80mm. A downward trend of the wall temperature is shown in Figure 5 e), since the leakage gas velocity increases with the radius. The lower wall temperature at the wheel centre (0-20mm) is particularly influenced by the shaft cooling temperature. In addition, the lower rotor outlet velocity (front: 1532m/s, back: 456m/s) and larger back face clearance (front: 2mm, back: 5mm) allow more working fluid flowing into the back gap (front: 0.056 kg/s, back: 0.107 kg/s). As shown in Figure 5 g), the leakage gas enters the middle of the wheel. Therefore, the wall temperature on the back side increases faster than the front (Figure 5 e)) due to the strong convective heat transfer effect.

An interesting phenomenon is that the temperature at the rotor blades (1021.9-1108.0 K) is lower than that of the wheel and shroud (≈1120 K). This is due to the high convective heat transfer coefficient and the heat generated at the non-working section can be quickly washed away, see in Figure 6 a). The partial admission ratio is approximately 0.33 for the investigated turbine. Therefore, the blade temperature is close to the non-working section. Besides, the temperature is not uniformly distributed along the radial direction (Figure 5 c) and d)), because the flow of the working section is extremely nonuniform (Figure 6 b)) and subsequently different heat transfer ability.

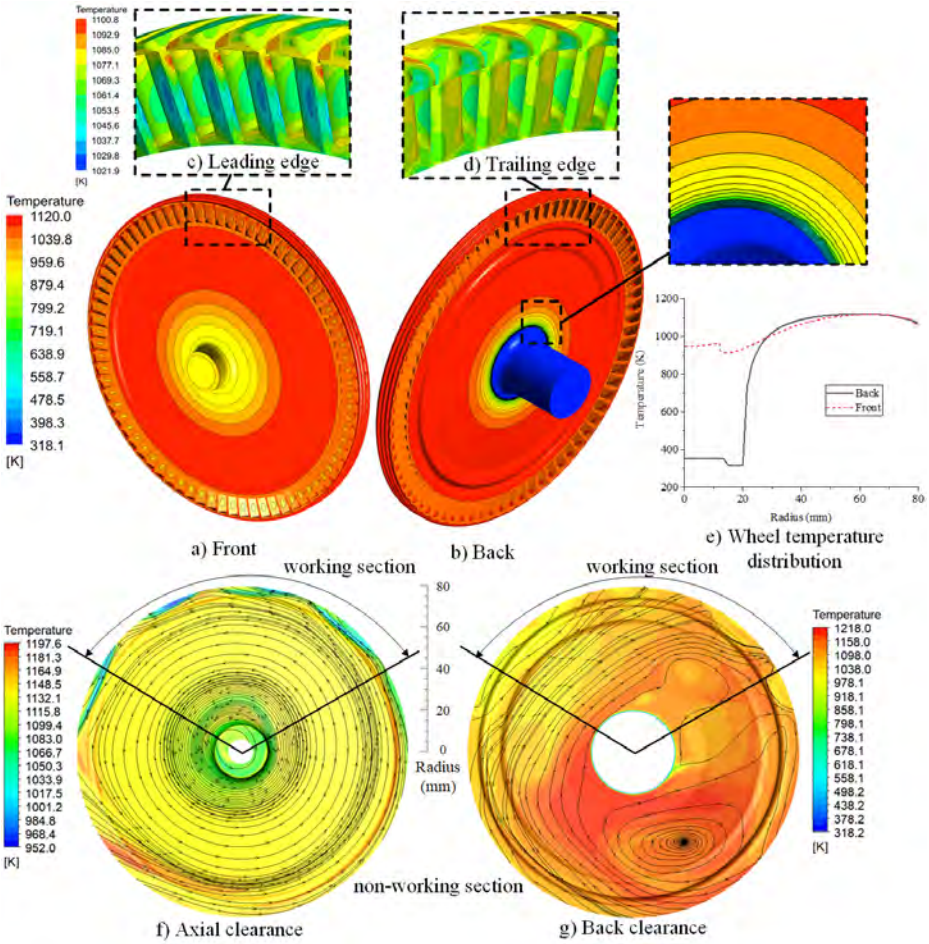

Figure 5 Temperature distribution

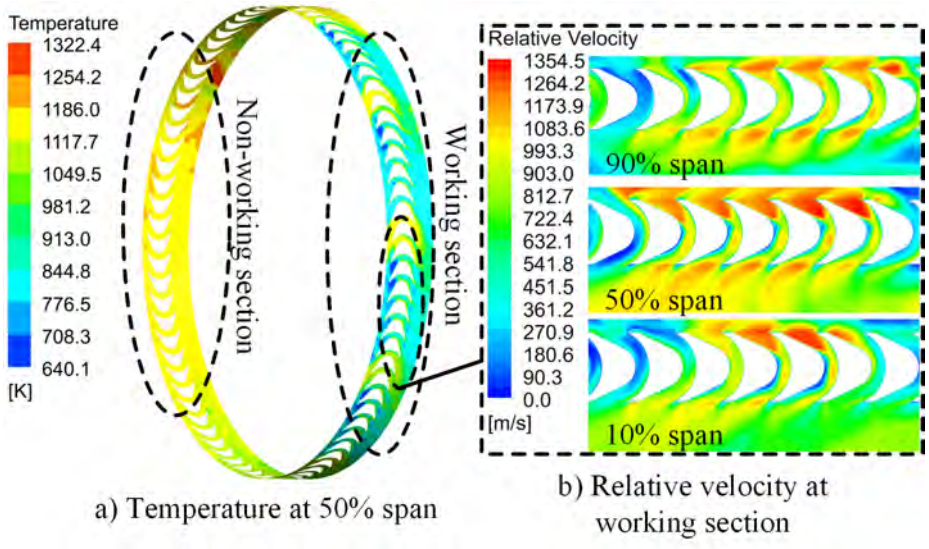

Figure 6 Flow characteristics

Stress and Deformation Analysis

In Table 2, five cases are selected to study the effect of pressure, rotation and temperature on the stress and deformation. Figure 7 illustrates the mechanical properties of the material. It provides the yield and fracture strength as a function of operating temperature.

Table 2 Load for Difference Cases

Load	Case 1	Case 2	Case 3	Case 4	Case 5
Pressure	√		√		√
Rotation		√	√		√
Temperature				√	√

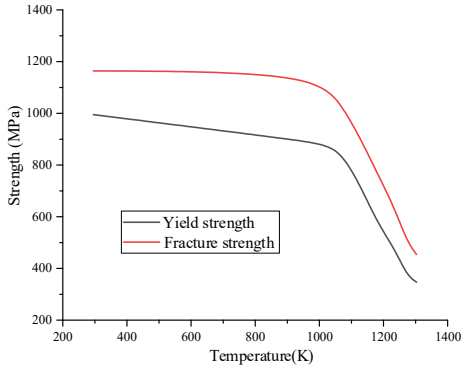

Figure 7 Variation of Yield Strength and Fracture Strength with Temperature

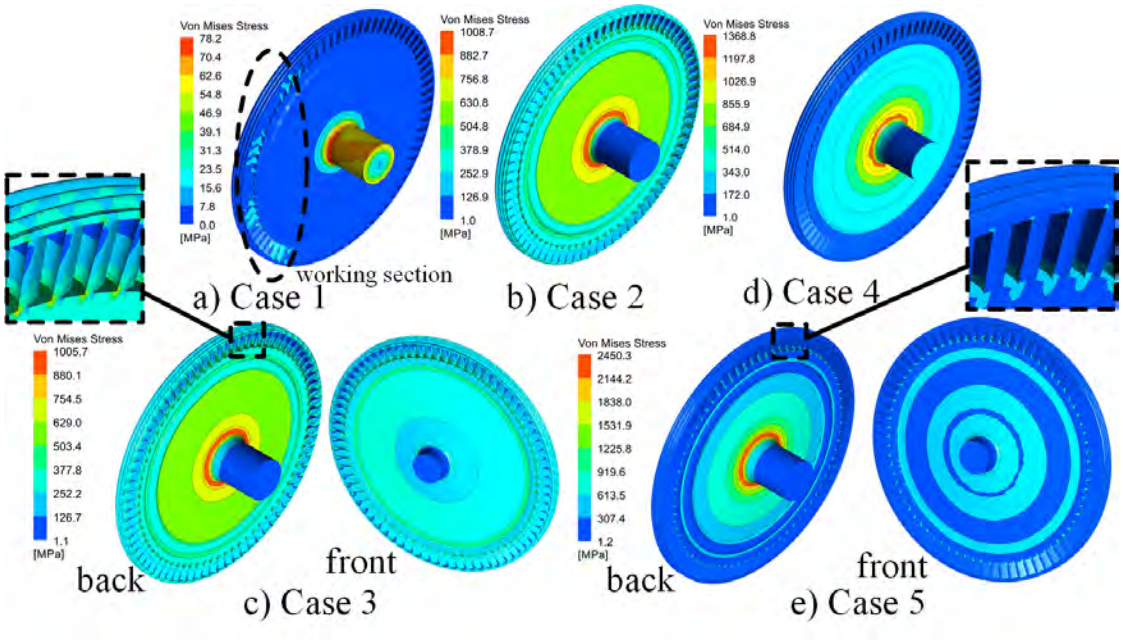

Figure 8 Distribution of Von Mises Stress

Figure 8 shows the results of the equivalent Von Mises stress due to different factors. The largest stress is located at the root of the wheel for all cases (Case 1: 78.2 MPa, Case 2: 1008.7 MPa, Case 3:1005.8 MPa, Case 4:1368.8 MPa, Case 5: 2450.3 MPa). As shown in Figure 5, the temperature at the root of the wheel is approximately 700 K. By not including the thermal stress, the material has entered to the plastic section due to pressure and centrifugal forces (Yield strength: 934 MPa; Fracture strength: 1160 MPa), see in Case 3. The materials can even exceed the fracture limit if the thermal stress is further considered, see in Case 5. The thermal stress is created due to the higher radial temperature gradient at the root of the wheel, as shown in Figure 5.

In addition, the stress of the blade root is also investigated. Due to the existence of shroud, the blade root now bears more centrifugal force. It is shown that the stress of blade root is almost 700 MPa (Case 3 and Case 5, see in Figure 8) and the temperature is approximately 1000 K (see in Figure 5). According to Figure 7, the stress at the blade root is lower than the yield limit and is within the safety range (Yield strength: 880 MPa; Fracture strength: 1102 MPa).

The influence of the aerodynamic forces on the stress is minimal and the centrifugal force is the critical by comparing Figure 8 a)-c) (Pressure load: 78.2 MPa; Rotation load: 1008.7 MPa; Pressure + Rotation load: 1005.7 MPa). Compared to

stress results in Figure 8 a), b) and d), it is found that the thermal stress is dominant in the total stress (Pressure load: 78.2 MPa; Rotation load: 1008.7 MPa; Temperature load: 1368.8 MPa). Therefore, it is necessary to reduce the radial temperature gradient at the turbine wheel by implementing proper cooling strategy.

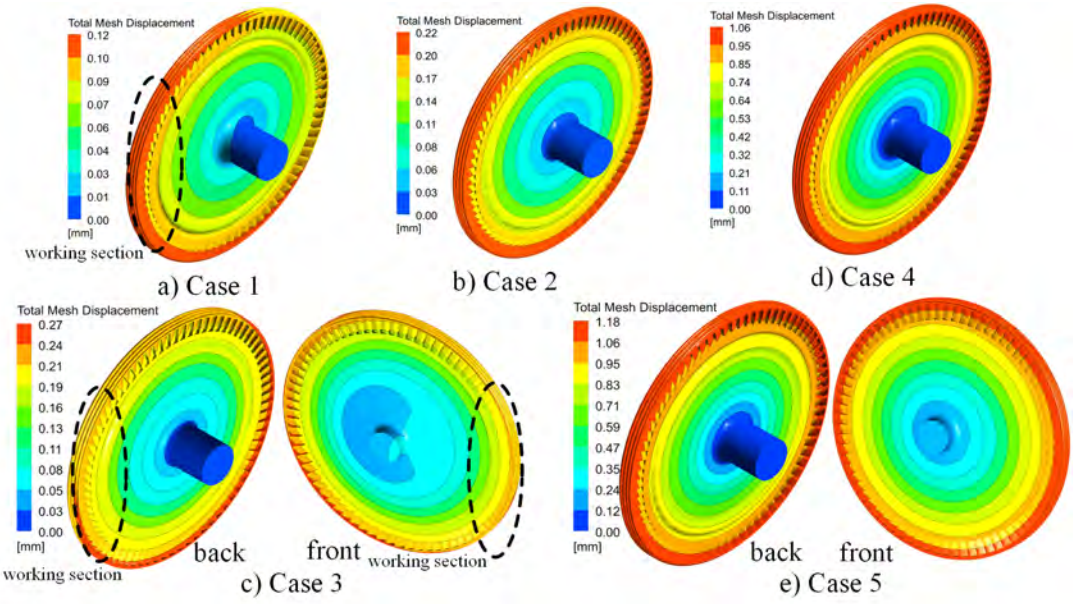

Figure 9 Distribution of total mesh displacement

Figure 9 shows the corresponding displacement distributions. The deformation is smeared circumferentially and gradually increases with the rotor radius as shown in Figure 9 b) and d). The maximum displacement is located at the shroud for Case 2 (0.22 mm) and Case 4 (1.06 mm) since the centrifugal force and thermal stresses are distributed uniformly in the radial direction. In addition, the rotor is not uniformly stressed due to the partial admission configuration if the thermal effects are not considered. Therefore, the deformation shown in Figure 9 a) and c) is not uniformly distributed in the radial direction. However, the maximum displacement is at the opposite position by comparing Case 1 and Case 3, because of the different acting directions of aerodynamic and centrifugal forces. As shown in Figure 9 (Case 3: 0.27 mm, Case 5: 1.18 mm), although the mechanical deformation is unevenly distributed, the total deformation is still distributed along the radial direction. It is also found that the thermally induced deformation is higher than other factors, therefore the thermally induced deformation is still the main cause compared to aerodynamic and mechanical forces. This further highlights the importance of reducing the temperature gradient at the turbine wheel.

CONCLUSIONS

This paper presents a fluid-thermal analysis of partial admission axial turbines. A two-way weakly fluid-thermal method is validated and is used to obtain the temperature distributions. The stress and deformation distributions are then investigated. The key findings are:

1) The rotor temperatures are smeared circumferentially due to the high-speed rotor rotation. One of the reasons is due to the viscous heating effects and the other is from working fluid flowing into the front and back gap. In addition, the temperature at the rotor blades is lower than the wheel and shroud due to the high convective heat transfer coefficient. Furthermore, the flow at the working section directly affects the temperature distribution on the blade surface.

2) The material has entered to the plastic section due to pressure and centrifugal forces. In addition, the material can even exceed the fracture limit if the thermal stress is further considered. Besides, due to the existence of shroud, the blade root bears more centrifugal force, but the blade root is still within the safety range. In addition, thermal stress is dominant in the total stress, reducing the radial temperature gradient at the wheel root is necessary.

3) The partial admission configuration causes ununiform mechanical deformation because the rotor is not uniformly stressed. In addition, the different directions of aerodynamic and centrifugal forces cause the opposite maximum deformation position for case 1 and case 3. However, the total deformation is still distributed along the radial direction by considering the temperature distribution, and the thermal deformation is still the main cause compared to mechanical and aerodynamic forces.

In summary, the turbine thermal performance can significantly influence strength and deformation of partial admission turbines. A proper cooling strategy is needed for the turbine operation in future.

NOMENCLATURE

E	Young's modulus	[GPa]

h	heat transfer coefficient	[W/m^2·K]
k	specific heat ratio	[-]
P	pressure	[Pa]
q	heat flux	[W/m^2]
R	gas constant; radius	[kJ/kg·K]; [mm]
T	temperature	[K]

Greeks

α	linear thermal expansion coefficient	[10^{-6}℃]
λ	thermal conductivity coefficient	[W/m·K]
μ	Poisson ratio	[-]
ρ	density	[g/cm^3]
ϕ	diameter	[mm]
ω	rotation speed	[RPM]

Subscripts

f	fluid
k	iteration steps
s	solid
w	wall

ACKNOWLEDGMENTS

The authors would like to thank the National Natural Science Foundation of China (NSFC) (Grant No. 51805435, 51909218) for the sponsorship.

REFERENCES

ANSYS (2017). *ANSYS user's guide releases 18.2*. Concord, MA, USA: ANSYS Inc.

Back, L.H., Massier, P.F., Gier, H.L. (1964). Convective Heat transfer in a Convergent-divergent Nozzle. *International Journal of Heat and Mass Transfer,* 7(5), pp. 549-568.

Bohn, D., Becker, V., Kusterer, K. (1999). 3-D Internal Flow and Conjugate Calculations of a Convective Cooled Turbine Blade with Serpentine-Shaped and Ribbed Channels. In: *Asme International Gas Turbine & Aeroengine Congress & Exhibition*. Indianapolis: ASME.

Bohn, D., Betcher, C., Kusterer, K., Weidtmann, K. (2021). Numerical and Analytical Investigation of Heat Transfer Mechanisms and Flow Phenomena in an IP Steam Turbine Blading During Startup. *Journal of Engineering for Gas Turbines and Power,* 143(2), pp. 21019.

Bunker, R.S. (2013). Turbine Heat Transfer and Cooling: An Overview. In: *Proceedings of the ASME Turbo Expo*. San Antonio: ASME.

DeLise, J., Naraghi, M. (1995). Comparative studies of convective heat transfer models for rocket nozzles. In: *31st Joint Propulsion Conference and Exhibit*. San Deigo: AIAA.

French, D.W. (2010). *Analysis of Unmanned Undersea Vehicle (UUV) architectures and an assessment of UUV integration into undersea applications*. Ph.D. Naval Postgraduate School.

Ju, Y., Feng, Y., Zhang, C. (2021). Conjugate Heat Transfer Simulation and Entropy Generation Analysis of Gas Turbine Blades. *Journal of Engineering for Gas Turbines and Power,* 8(143), pp. 81012.

Marineau, E.C., Schetz, J.A., Neel, R.E. (2006). Turbulent Navier-Stokes Simulations of Heat Transfer with Complex Wall Temperature Variations. In: *9th AIAA/ASME joint thermophysics and heat transfer conference*. San Francisco: AIAA/ASME.

Moustapha, H., Zelesky, M.F., Baines, N.C., Japikse, D. (2003). *Axial and radial turbines*. White River Junction, VT: Concepts NREC.

Qin, K., Jacobs, P.A., Keep, J.A., Li, D., Jahn, I.H. (2018). A Fluid-structure-thermal Model for Bump-type Foil Thrust Bearings. *Tribology International,* 121, pp. 481-491.

Qin, K., Wang, H., Wang, X., Sun, Y., Luo, K. (2020). Thermodynamic and Experimental Investigation of a Metal Fuelled Steam Rankine Cycle for Unmanned Underwater Vehicles. *Energy Conversion and Management,* 223, pp. 113281.

Rigby, D.L., Lepicovsky, J. (2001). Conjugate Heat Transfer Analysis of Internally Cooled Configurations. In: *ASME Turbo Expo 2001: Power for Land, Sea, and Air*. New Orleans: ASME.

Shrestha, S.K., Kim, D., Kim, Y.C. (2013). Experimental Feasibility Study of Radial Injection Cooling of Three-Pad Air Foil Bearings. *Journal of Tribology,* 135(4), pp. 41703.

Wang, H., Chao, Y., Tang, T., Luo, K., Qin, K. (2021). A Comparison of Partial Admission Axial and Radial Inflow Turbines for Underwater Vehicles. *Energies,* 14(5), pp. 1514.